Volume 9
Number 33
7 September 2021
Pages 10507–10986

Journal of Materials Chemistry C

Materials for optical, magnetic and electronic devices

rsc.li/materials-c

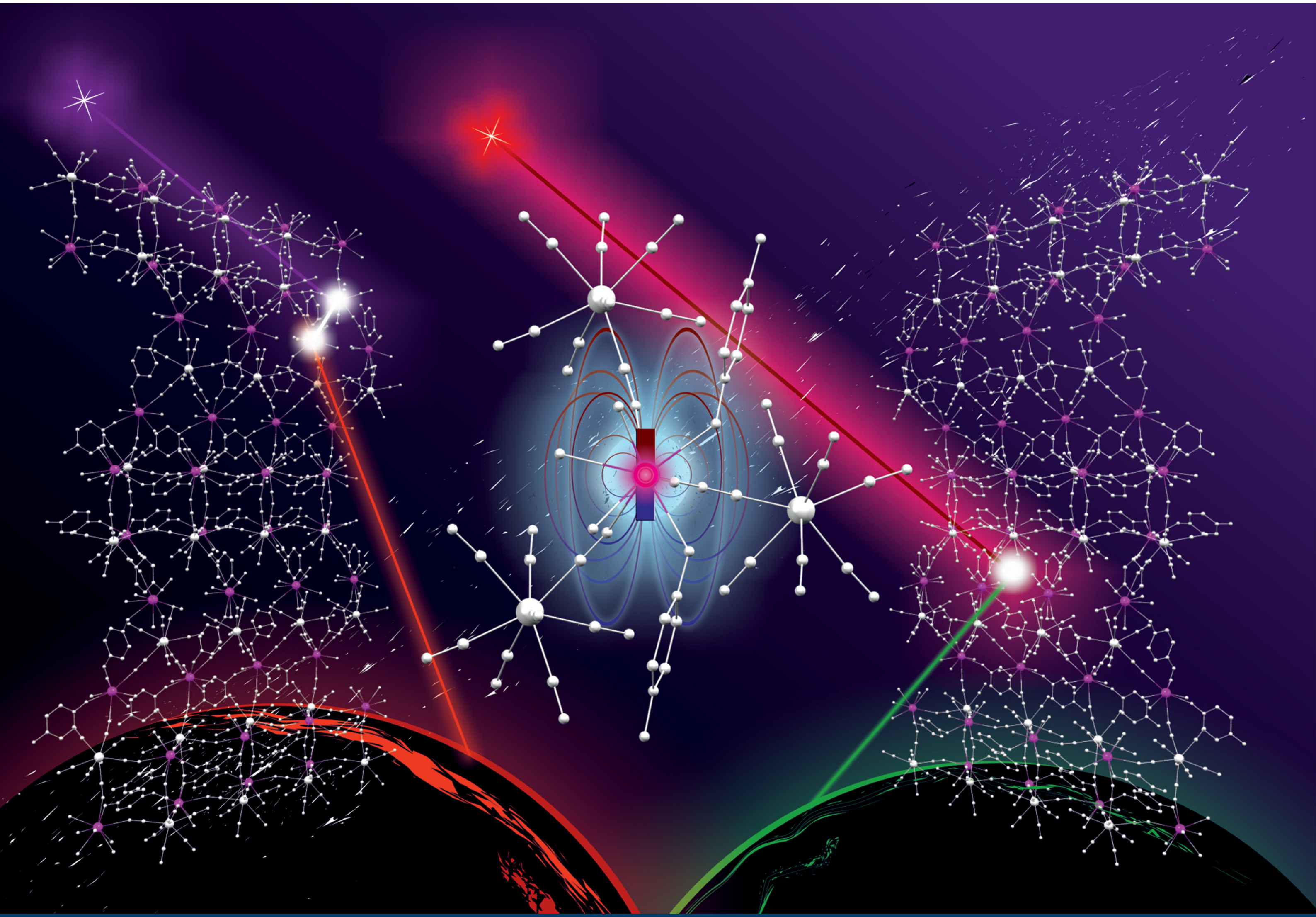

Themed issue: Materials for molecular electronics and magnetism

ISSN 2050-7526

ROYAL SOCIETY OF CHEMISTRY

PAPER

Shin-ichi Ohkoshi, Szymon Chorazy, Barbara Sieklucka *et al.*
SHG-active NIR-emissive molecular nanomagnets generated in layered neodymium(III)–octacyanidometallate(IV) frameworks

Journal of
Materials Chemistry C

ROYAL SOCIETY
OF CHEMISTRY

PAPER

View Article Online
View Journal | View Issue

Check for updates

Cite this: *J. Mater. Chem. C*, 2021, **9**, 10705

SHG-active NIR-emissive molecular nanomagnets generated in layered neodymium(III)–octacyanidometallate(IV) frameworks†

Robert Jankowski,[a] Jakub J. Zakrzewski,[a] Mikolaj Zychowicz,[a] Junhao Wang,[b] Yurie Oki,[b] Shin-ichi Ohkoshi,*[b] Szymon Chorazy*[a] and Barbara Sieklucka*[a]

Received 20th February 2021,
Accepted 16th April 2021

DOI: 10.1039/d1tc00825k

rsc.li/materials-c

Lanthanide(III) single-molecule magnets (Ln-SMMs) offer the fruitful conjunction of magnetic and photoluminescent properties originating from their single-ion anisotropy and emissive f–f electronic transitions. The flexibility of lanthanide(III)-based coordination systems is the most significant prerequisite for the generation of additional physical phenomena, including non-linear optical effects related to the lack of inversion centre. In the quest towards multifunctional molecular nanomagnets, we report heterometallic d–f layered coordination polymers, $\{[\mathrm{Nd^{III}}_4(\mathrm{H_2O})_{17}(\mathrm{pzdo})_5][\mathrm{M^{IV}(CN)_8}]_3\}\cdot 9\mathrm{H_2O}$ (M = Mo (**1**), W (**2**); pzdo = pyrazine-*N*,*N*′-dioxide). They crystallize in the non-centrosymmetric *C*2 space group due to the spontaneous resolution process, confirmed by the observation of second harmonic generation (SHG) activity. These materials exhibit UV-to-vis-light-induced near-infrared (NIR) $\mathrm{Nd^{III}}$-centred luminescence sensitized by octacyanidometallates and organic ligand, and slow relaxation of magnetization of $\mathrm{Nd^{III}}$ complexes which was investigated by alternate-current (ac) magnetic measurements and the *ab initio* calculations. The observed magnetic and optical properties are sensitive to the nature of the d-transition metal centre, namely most of their features are improved upon the replacement of $\mathrm{Mo^{IV}}$ with $\mathrm{W^{IV}}$ centres. In this work, we show the generation of SHG-active NIR-emissive SMMs realized by $\mathrm{Nd^{3+}}$ ions inserted into hybrid layers built of inorganic $[\mathrm{M(CN)_8}]^{4-}$ and organic pzdo linkers.

Introduction

Single-molecule magnets (SMMs) constitute a class of paramagnetic metal complexes whose magnetic anisotropy results in a slow magnetic relaxation effect.[1] At the low-temperature regime, SMMs retain their magnetization for a long time in the absence of an external magnetic field. This gives a magnetic bistability effect opening applications for high-density data storage and processing devices.[2] Moreover, quantum phenomena such as quantum tunnelling of magnetization or quantum coherence are observed in molecular nanomagnets extending the interest in SMMs toward molecular spintronics and quantum computation.[3] The first generation of SMMs was based on 3d metal clusters with a high-spin of the ground state.[1] It was later established that single-ion anisotropy plays a key role in achieving high-performance SMMs,[4] thus the attention has been shifted to SMMs based on lanthanide(3+) ions showing strong magnetic anisotropy related to the contributions from spin–orbit coupling and crystal field effects.[5] The construction of molecular nanomagnets built of intrinsically emissive lanthanide(III) centres implied the emergence of luminescent SMMs which expand the application scope toward light-emitting devices, optical sensors or thermometers.[6] For the last decade, emissive SMMs, exploring mainly $\mathrm{Dy^{III}}$ and $\mathrm{Yb^{III}}$, have attracted considerable attention which was also connected with the magneto-optical correlations exploring the usage of emission spectra in the investigation of lanthanide(III) electronic structure.[7] Moreover, emissive SMMs are candidates for magneto-optical systems that can realize the tuning of emission by a magnetic field.[8] It was recently shown that the rich coordination chemistry of lanthanide ions enables further functionalization of luminescent SMMs toward high proton conductivity or ferroelectricity.[9]

In these regards, the objective of our work was to employ luminescent SMMs for the construction of unique multifunctional materials. We focused on the generation of chirality in

---

[a] *Faculty of Chemistry, Jagiellonian University, Gronostajowa 2, 30-387 Krakow, Poland. E-mail: chorazy@chemia.uj.edu.pl, barbara.sieklucka@uj.edu.pl*

[b] *Department of Chemistry, School of Science, The University of Tokyo, 7-3-1 Hongo, Bunkyo-ku, Tokyo 113-0033, Japan. E-mail: ohkoshi@chem.s.u-tokyo.ac.jp*

† Electronic supplementary information (ESI) available: IR spectra. TGA curves. Additional structural parameters and views. Results of continuous shape measure analysis. P-XRD patterns. Scheme of the experimental setup used for the SHG experiment. Additional SHG characteristics. Solid-state UV-vis absorption spectra. Additional magnetic characteristics. Detailed results of the *ab initio* calculations and their correlation with the emission spectra. CCDC 2061390 and 2061391 for **1a** and **1b**, respectively. For ESI and crystallographic data in CIF or other electronic format see DOI: 10.1039/d1tc00825k

the emissive SMM-based systems. This goal is motivated by the broad range of effects that can be induced thanks to the chirality or at least the non-centrosymmetric character of the crystals. It is worth mentioning second harmonic generation (SHG),[10] circularly polarized luminescence (CPL),[11] both with the magnetic enhancement (MSHG/MCPL), or even more advanced magneto-chiral dichroism (MChD).[12]

To achieve photoluminescent SMMs crystalizing in the non-centrosymmetric space group, we decided to explore heterometallic d–f cyanido-bridged assemblies. It was shown that polycyanidometallates can enhance lanthanide luminescence and constitute a useful tool to adjust the geometry of 4f metal ions towards the SMM behaviour.[13] Furthermore, the application of cyanido metal complexes with functionalized organic ligands is an effective strategy for chiral and non-centrosymmetric materials revealing SHG, MSHG, or MChD phenomena.[14] Following this perspective, we selected Nd^{3+} ions combined with $[M(CN)_8]^{4-}$ (M = Mo^{IV}, W^{IV}) metalloligands accompanied by pyrazine-*N*,*N*′-dioxide (pzdo) as a supporting organic linker. The Nd^{III} centres are rarely used for SMMs due to moderate single-ion anisotropy and relatively low magnetic moment. However, similarly to commonly used Dy^{3+} ions, they are characterized by oblate electron density, thus the negatively charged ligands giving axial crystal field are the key to high-performance molecular nanomagnets, supported by symmetry and/or magnetic isolation.[5b,15] Moreover, they offer a straightforward route to emissive materials as they exhibit efficient near-infrared (NIR) luminescence.[16] On the other hand, diamagnetic $[M(CN)_8]^{4-}$ (M = Mo^{IV}, W^{IV}) ions can not only ensure magnetic isolation of 4f metal ions enabling observation of SMM behaviour but also, when combined with pzdo ligands, they can form anion–π aggregates which are suitable for the sensitization of lanthanide NIR emission.[17] Although the generation of chirality by a spontaneous resolution process is extremely hard to predict, it is usually related to the formation of the specific supramolecular interactions during the crystals growth.[18] Therefore, rich contacts involving cyanido ligands can play a non-innocent role in the spontaneous resolution effect producing chiral molecular systems.[14a,19] Actually, the {pzdo-$[M(CN)_8]^{n-}$} aggregates can be promising in this context.[17,20] Thanks to all these rationally selected molecular building blocks, we report two novel layered coordination polymers, $\{[Nd_4(H_2O)_{17}(pzdo)_5][M^{IV}(CN)_8]_3\}\cdot 9H_2O$ (M = Mo (**1**), W (**2**)) crystallizing in a non-centrosymmetric *C*2 space group. They are multifunctional, exhibiting SHG activity, sensitized NIR emission, and slow magnetic relaxation effects. All these

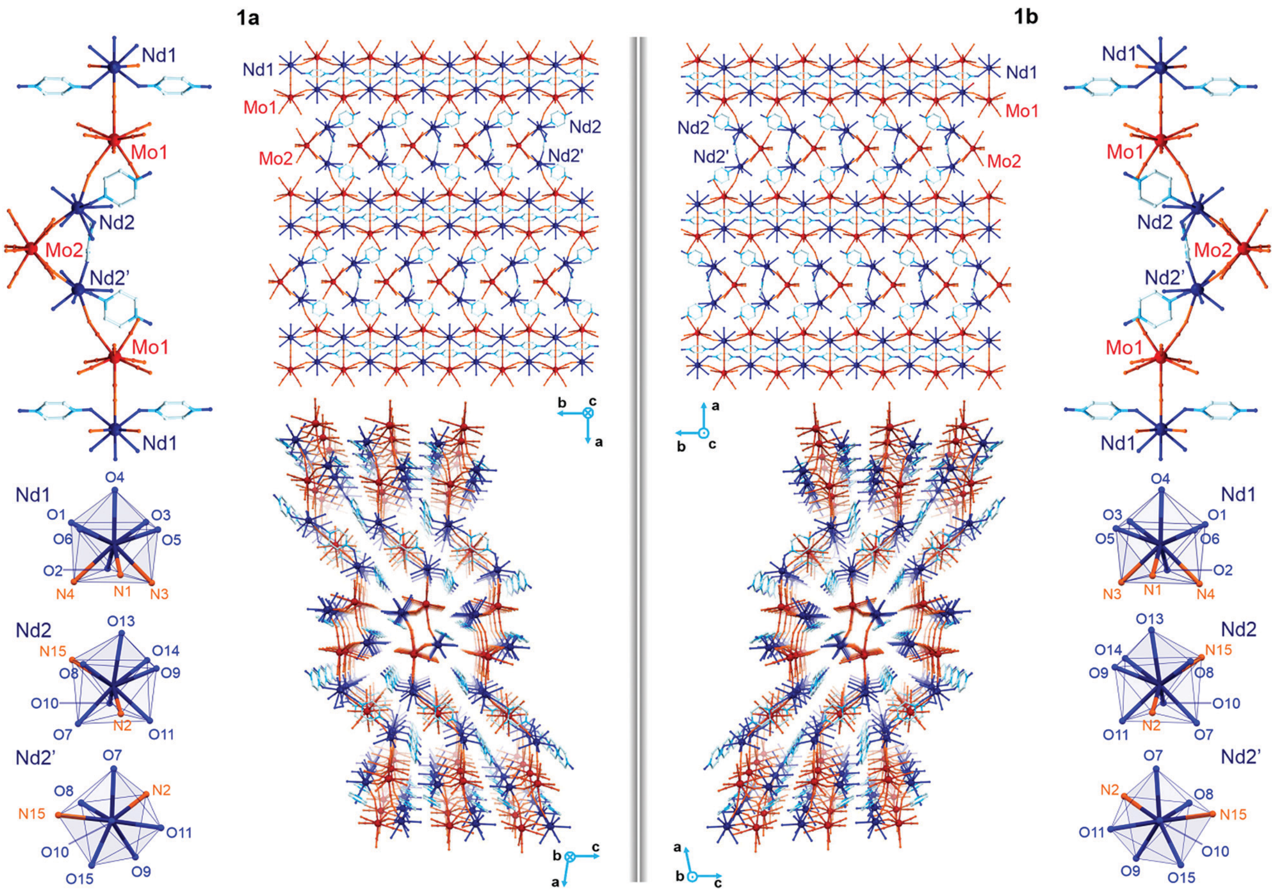

Fig. 1 Representative views of the crystal structures of **1a** (left side) and **1b** (right side) including the crystal packing along the *c* (middle top) and *b* (middle bottom) crystallographic axes, molecular building units (top corners), and coordination spheres of three non-equivalent Nd complexes (bottom corners). A solvent of crystallization was omitted for clarity.

properties are tuned by the $[M^{IV}(CN)_8]^{4-}$ molecular building block as shown by thorough structural, luminescence, non-linear optical, and magnetic studies, supported by the *ab initio* calculations.

Results and discussion

Structural studies

The yellow plate crystals of $\{[Nd_4(H_2O)_{17}(pzdo)_5][Mo^{IV}(CN)_8]_3\}\cdot 9H_2O$ (**1**) were obtained from the H_2O/MeOH solution by the self-assembly of Nd^{3+} cations, $[Mo^{IV}(CN)_8]^{4-}$ anions, and pyrazine-*N*,*N*′-dioxide (pzdo). The W^{IV} analogue $\{[Nd_4(H_2O)_{17}(pzdo)_5][W^{IV}(CN)_8]_3\}\cdot 9H_2O$ (**2**) was prepared in an analogous manner using $[W(CN)_8]^{4-}$ anions, which resulted in the orange polycrystalline sample. Obtained compounds were preliminarily characterized by the CHN elemental analysis, IR spectra, and TGA (Fig. S1 and S2, ESI,† and Experimental section), and, afterwards by the X-ray diffraction methods (Fig. 1, 2, Fig. S3–S5, and Tables S1–S4, ESI†). The single-crystal XRD experiment indicates that **1** crystallizes in the non-centrosymmetric *C*2 space group as the mixture of enantiomorphic crystals, hereinafter referred to as **1a** and **1b** (Fig. 1 and Table S1, ESI†). The crystals of **2** were too small to perform the SC-XRD experiment but the powder XRD (P-XRD) technique confirmed its isostructurality with **1** (Fig. 2). Compounds **1** and **2** are constructed of layered cyanido-bridged frameworks accompanied with interlayer water of crystallization (Fig. 1), resulting in a composition of $\{[Nd_4(H_2O)_{17}(pzdo)_5];[M^{IV}(CN)_8]_3\}\cdot 9H_2O$, M = Mo (**1**), W (**2**), crystallographically represented by two types of Mo centres (Mo1 and Mo2) and three types of Nd centres (Nd1, Nd2, Nd2′). The single coordination layer of **1a** is composed of cyanido-bridged ladder-like assemblies formed by the conjugation of $\{Mo1_2Nd1_2\}$ square units. They are stabilized by the co-existing {Nd1–pzdo–Nd1} linkages which form metal–organic chains positioned above and below the plane of the ladders. The coordination ladders are further linked along a two-fold screw axis through {Nd2–Mo2–Nd2′} triangular fragments which are supported by the local {Nd2–pzdo–Nd2′} linkages. These trinuclear $\{Nd_2Mo_1(pzdo)\}$ spacers between ladder-type assemblies are intrinsically non-centrosymmetric which is related to the specific alignment of $[Mo2(CN)_8]^{4-}$ ions above the pzdo. This contributes to the chirality of the whole coordination network as the alignment of {Nd2–Mo2–Nd2′} triangles, which are decorated by terminal pzdo ligands, in **1a** is a mirror image of the analogous arrangement observed in **1b** (Fig. 1). The formation of such a chiral structure was also enabled by the specific 4 : 3 stoichiometry of Nd : Mo as suggested by our recent report on the related ErYb(pzdo)–MoW coordination systems bearing organic counterions leading to the simple 1 : 1 metal ratio and the centrosymmetric structure.[17] The structural comparison between **1** and **2**, and other reported Ln^{III}–$[M^{IV}(CN)_8]$ systems crystallizing in the centrosymmetric space groups, are gathered in Table S5 (ESI†).

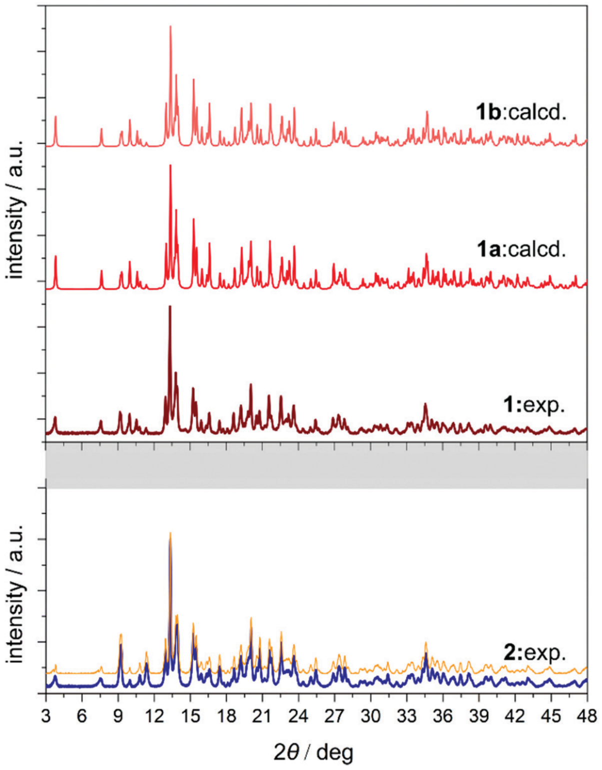

Fig. 2 Comparison of the experimental powder X-ray diffraction (P-XRD) pattern measured for **1** with the patterns for **1a** and **1b** calculated based on structural models obtained from the SC-XRD method (top), together with the experimental P-XRD pattern gathered for **2** which was compared with the pattern (orange line) obtained from the LeBail fitting procedure performed using EXPO 2014 software (bottom).

The asymmetric units of **1a** and **1b** contain four cyanido-bridged metal centres, two Mo (Mo1/Mo2) centres and two Nd (Nd1/Nd2) centres, accompanied by water molecules of crystallization (Fig. S3, ESI†). However, a static structural disorder concerning the pzdo ligand attached to the Nd2 centre was found, which results in the presence of two distinguishable Nd2 and Nd2′ sites, both existing with the 0.5 occupancies (Fig. S3 and S4, ESI†). Taking this into account, the molecular building unit for **1a** and **1b** can be defined as the seven-metallic fragment consisting of three $[Mo(CN)_8]^{4-}$ ions (two Mo1 and one Mo2 centres) alternately arranged with four Nd^{III} complexes (two Nd1, one Nd2, and one Nd2′ centres). The coordination sphere of Nd1 is filled with three N-atoms of the {Mo–CN–Nd} molecular bridges, four aqua ligands, and two O-atoms of bridging pzdo ligands. The Nd2/Nd2′ coordination sphere involves, apart from two N-atoms of cyanido bridges and two pzdo ligands, five or four aqua ligands, depending on the pzdo ligand position. The nine-coordinated Nd2 complex reveals five aqua ligands, while four aqua ligands are attached to eight-coordinated Nd2′ sites. All Mo^{IV} complexes are eight-coordinated bearing three (Mo1) or two (Mo2) cyanido ligands participating in the formation of cyanido bridges. The remaining cyanido ligands are terminal. To precisely determine the coordination geometry of Nd^{III} and Mo^{IV} complexes in **1a** and **1b**, a Continuous Shape Measure (CShM) analysis was performed (Table S2, ESI†).[21] It indicates that all $[Mo(CN)_8]^{4-}$ complexes reveal the geometry close to an ideal square antiprism. The nine-coordinated Nd1 complex exhibits the geometry close to a tricapped trigonal prism, the Nd2 centre adopts the intermediate geometry between a tricapped trigonal prism and a capped square antiprism, while the eight-coordinated Nd2′ centre can be assigned to a triangular dodecahedron. Besides the coordination connectivity, the crystal structures of **1a** and **1b** are stabilized by a series of non-covalent interactions. The noticeable role is played by the anion–π aggregates involving negatively charged $[Mo(CN)_8]^{4-}$ ions, and electron-deficient aromatic rings of pzdo ligands. They contribute to the stabilization of a chiral structure as they are not only observed within coordination ladders but also induce the directional alignment of {Nd2–Mo2–Nd2′} triangles within the hybrid coordination layers (Fig. 1 and S6, ESI†). On the other hand, the neighbouring layers are separated by the rich hydrogen bonding network employing water molecules of crystallization, aqua ligands of Nd^{III} complexes, and terminal cyanido ligands of Mo^{IV} centres. The shortest distance between neodymium ions of neighbouring layers is 6.7 Å which is also the closest Nd···Nd distance in the whole structure. The closest intralayer Nd···Nd contact is 7.4 Å. Taking into account all structural parameters, **1a** and **1b** are the perfect mirror images (Fig. 1, Tables S1–S3, ESI†), being a pair of enantiomorphs as confirmed by the low values of 0.025(8) and 0.024(8) of the respective Flack parameters. However, as stated above, **1** grows as the mixture of enantiomorphic crystals, **1a** and **1b**, which hampered the additional characterization of the generated structural chirality by circular dichroism spectroscopy. The isostructurality of **1a** and **1b**, and their phase purity were checked by the P-XRD patterns (Fig. 2). The P-XRD method also indicates the isostructurality of **2** with almost identical unit cell volume and parameters (Fig. 2 and Fig. S5, Table S4, ESI†).[22]

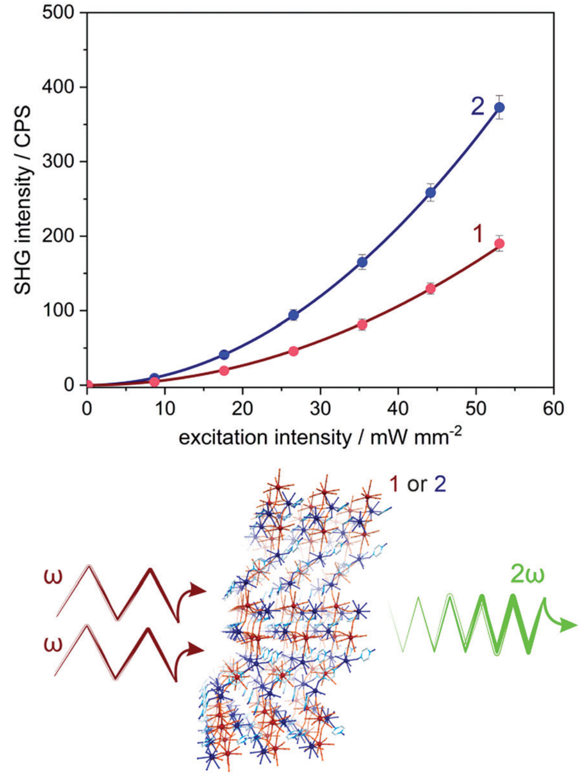

Fig. 3 The room-temperature SHG intensity of **1** and **2** in the function of excitation intensity (top) together with a schematic illustration of the SHG effect (bottom). The 1040 nm laser source was used so as the green 520 nm light was investigated as the output SHG signal. The coloured circular points represent the experimental data while solid lines show the best-fits following the quadratic function.

SHG activity

Owing to the non-centrosymmetric *C*2 space group (Table S1, ESI†), **1** and **2** can be considered as promising materials for the observation of non-linear optical (NLO) properties. To examine this perspective, the measurement of the second harmonic generation (SHG) was performed. The SHG phenomenon is related to the interaction of photons of the *ω* frequency with solid lacking inversion symmetry, which gives rise to the frequency doubling (2*ω*) effect. The scheme illustrating the homemade setup used for the SHG experiment was presented in Fig. S7 (ESI†) (for details, see the Experimental section). The polycrystalline samples of **1** and **2** were irradiated using a 1040 nm femtosecond pulse laser as incident fundamental light. Subsequently, the second harmonic green light of *ca.* 520 nm was investigated (Fig. S8, ESI†). The intensity of recorded SH light was found to be proportional to the square of the excitation light intensity, indicating the two-photon process characteristic of the SHG effect (Fig. 3 and Fig. S9, ESI†).[23] To quantify the SHG response from **1** and **2**, the well-known SH reference of potassium dihydrogen phosphate (KDP) was measured under identical experimental conditions (Fig. S8 and S9, ESI†). The intensities of the SHG light in **1** and **2** were found to be rather small, reaching 0.11% of KDP for **1** and 0.22% of KDP for **2**. The noticeable difference in the SHG response between **1** and **2** can be assigned to the small variation of an ionic size radius and the change in polarizability occurring with the transition metal substitution from Mo to W centres.[24]

Light absorption and photoluminescence studies

The powder samples of **1** and **2** exhibit intense yellow and orange colours, respectively, and contain Nd^{III} complexes whose relatively strong near-infrared photoluminescence was broadly explored.[25] Therefore, the obtained compounds were investigated using solid-state UV-vis-NIR absorption and photoluminescence spectra (Fig. 4 and Fig. S10, ESI†). In the visible region of the absorption spectra of **1** and **2**, the series of weak peaks are observed (Fig. S10, ESI†). They can be assigned to the f–f electronic transitions of Nd^{III} centres, from the ground $^4I_{9/2}$ multiplet to the higher-lying energy levels.[25] At higher energies, much stronger broad absorption bands, ranging from the UV region to *ca.* 550 nm for **1** and even *ca.* 600 nm for **2**, are observed. They were deconvoluted into five main components (Fig. S10, ESI†). Four of them, covering the UV-vis range to *ca.* 450 nm, are positioned at very similar energy positions in **1** and **2** (Table S6, ESI†), as they originate from the combined contributions from the singlet-to-singlet n–π* and π–π* transitions of pzdo ligands, and the transitions from the ligand-field (LF) and metal-to-ligand charge transfer (MLCT) electronic states of

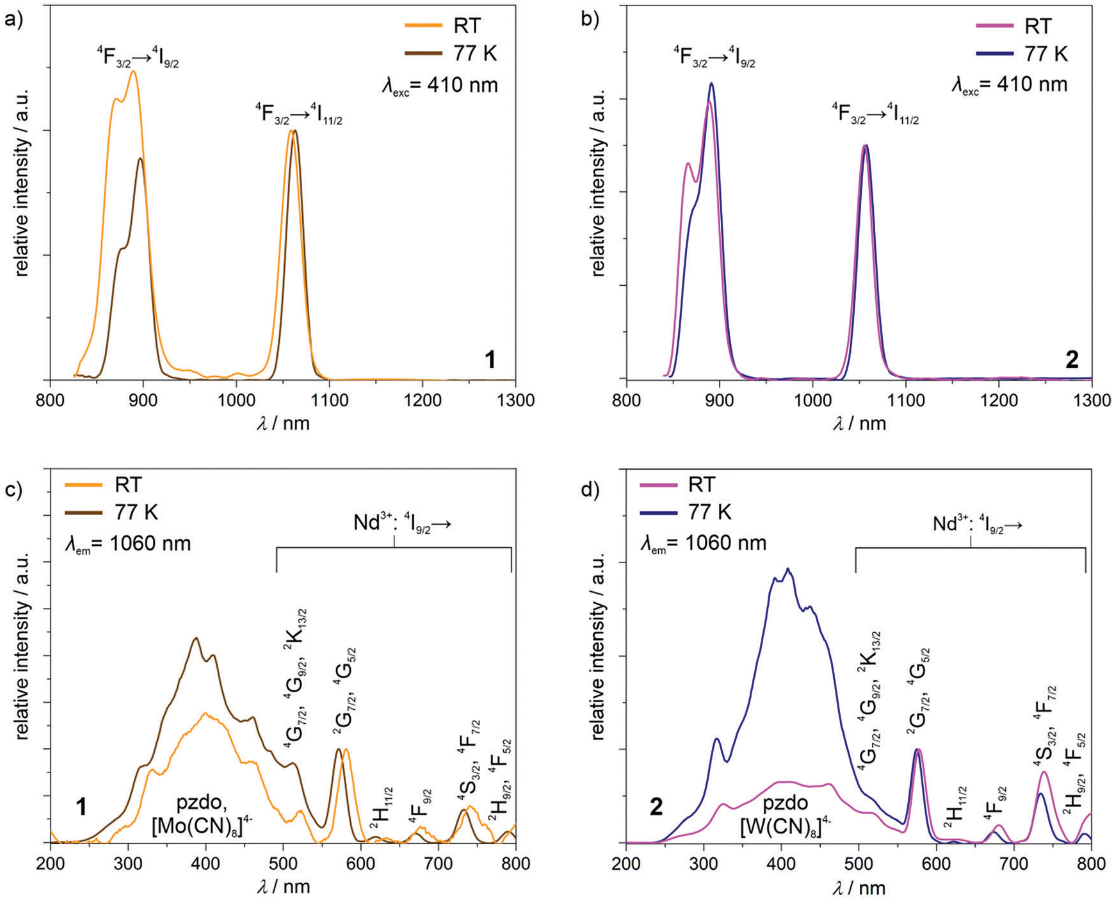

Fig. 4 Solid-state photoluminescence properties of **1** and **2**: emission spectra under the 410 nm excitation light for **1** (a) and **2** (b), together with the related excitation spectra for the monitored emission at 1060 nm for **1** (c) and **2** (d). The spectra at room temperature (RT) and liquid nitrogen temperature (77 K) were shown in each case. The assignments of the main emission and excitation bands to the incorporated molecular building blocks (pzdo, $[M(CN)_8]^{4-}$, Nd^{3+} ions with their f–f electronic transitions) were shown.

octacyanidometallate anions.[26] The LF states are also mainly responsible for the last deconvoluted component lying in the visible range. However, this absorption band is significantly broadened beyond the expected limit for the electronic transitions of $[M(CN)_8]^{4-}$ ions. This is particularly visible in **2** (Fig. S10d, ESI†). Therefore, the additional contribution to these bands should be postulated. It can be ascribed to the appearance of the anion–π CT states which were recognized for the coordination systems involving pzdo–$[M^{IV}(CN)_8]^{4-}$ (M = Mo, W) moieties.[17]

Using the light irradiation with wavelength below *ca.* 600 nm, the powder samples of **1** and **2** exhibit the distinct emission signal lying in the NIR region, easily detectable at room temperature (Fig. 4a and b). The emission patterns consist of two sharp peaks positioned at 890 and 1059 nm, and 886 and 1055 nm for **1** and **2**, respectively. They can be assigned to the Nd^{III}-centred f–f electronic transitions from the emissive $^4F_{3/2}$ excited state to the $^4I_{9/2}$ and $^4I_{11/2}$ multiplets.[25] Lowering the temperature to 77 K results in a very small red-shift of these maxima which is typical for the emission related to the 4f electronic levels well-shielded by 4d and 5s shells. To examine how the observed emission is realized after the light absorption, the excitation spectra for the monitored main emission peak at 1060 nm was examined at room and liquid nitrogen temperatures (Fig. 4c and d). For both **1** and **2**, the excitation pattern consists of a series of sharp peaks in the visible range, which are ascribable to the well-defined f–f electronic transitions indicating the direct f–f excitation pathway. However, the additional broad band is present in the UV-vis region up to *ca.* 600 nm. By comparison with the absorption spectra (Fig. S10, ESI†), it can be assigned to the electronic transitions within the pzdo ligands, $[M^{IV}(CN)_8]^{4-}$ (M = Mo, W) moieties, and their anion–π CT states. Therefore, they represent the NIR Nd^{III}-centred emission realized by the energy transfer process exploring both ligand-to-metal and metal-to-metal routes.[17,25] To deeply discuss the observed emission sensitization effect, the excitation spectra were normalized to the maximum of the direct f–f excitation band at 570 nm (Fig. 4c and d). At room temperature, for both **1** and **2**, the UV-to-vis excitation band related to the energy transfer process is at a similar level as the direct f–f excitation band lying above 550 nm. This indicates that both types of excitation pathways are similarly efficient despite much stronger UV-light absorption. This means that only the part of energy absorbed by pzdo and $[M^{IV}(CN)_8]^{4-}$ is transferred to Nd^{III} centres while the significant part is lost through the non-radiative deactivation. However, at a decreased temperature, the energy transfer route becomes dominant over the direct f–f excitation which can be ascribed to the hampering of deactivation processes *e.g.* through thermally activated vibrations, and to the cancelling of the thermally-assisted back energy transfer (BET) process.[17,25] In this context, there is a noticeable difference between the obtained compounds. Both at room temperature and 77 K, **1** exhibits the energy transfer excitation stronger than the direct f–f excitation, and the lowering of temperature increases the excitation intensity ratio (Fig. 4c). On the contrary, for **2**, the room-temperature excitation band in the 250–600 nm range is weaker than the strongest peaks of direct f–f excitation but this compound shows much stronger temperature dependence producing better emission sensitization at 77 K (Fig. 4d). This can be mainly explained by the role of thermally-activated BET mechanism from the excited states of Nd^{III} to the donor states of $[M^{IV}(CN)_8]^{4-}$ moieties.[27] This unfavourable effect seems to be more efficient in **2** due to the presumably closer distance between the acceptor state and the donor electronic states of the cyanido complexes. However, when at 77 K the BET is quenched, the smaller energy difference leads to more efficient sensitized emission. This interpretation stays in line with the related absorption spectra showing the longer wavelength tail of the main broad band in **2** (Fig. S10c and d, ESI†).

Magnetic properties

Due to the presence of Nd^{III} paramagnetic centres, which may exhibit the effect of slow relaxation of magnetization,[5b,15] **1** and **2** were investigated by direct-current (dc) and alternate-current (ac) magnetic measurements (Fig. 5 and Fig. S11–S17, ESI†). For both materials, the $\chi_M T$ products at room temperature, 6.36 and 6.30 cm^3 mol^{-1} K for **1** and **2**, respectively, are close to the expected values for four uncoupled Nd^{3+} ions (Fig. S11a, ESI†).[5b,15] Upon cooling, a gradual decrease of $\chi_M T$ product is observed, which is mainly the result of thermal depopulation of m_J states within the $^4I_{9/2}$ ground multiplet. The featureless course of the $\chi_M T(T)$ curve excludes the presence of significant magnetic interactions proving the sufficient isolation of Nd^{III} complexes by diamagnetic octacyanidometallate and pzdo linkers. The field dependences of magnetization measured at 1.8 K exhibit a monotonous increase of the signal to 5.43 and 5.39 μ_B at 70 kOe, for **1** and **2**, respectively, without any sign of magnetic hysteresis observable for high-performance SMMs (Fig. S11b, ESI†).[2]

At 1.8 K, both **1** and **2** subjected to a small field of 200 Oe start to reveal the non-zero signal of the out-of-phase magnetic susceptibility, χ'' under variable ac frequency (Fig. 5a, b and

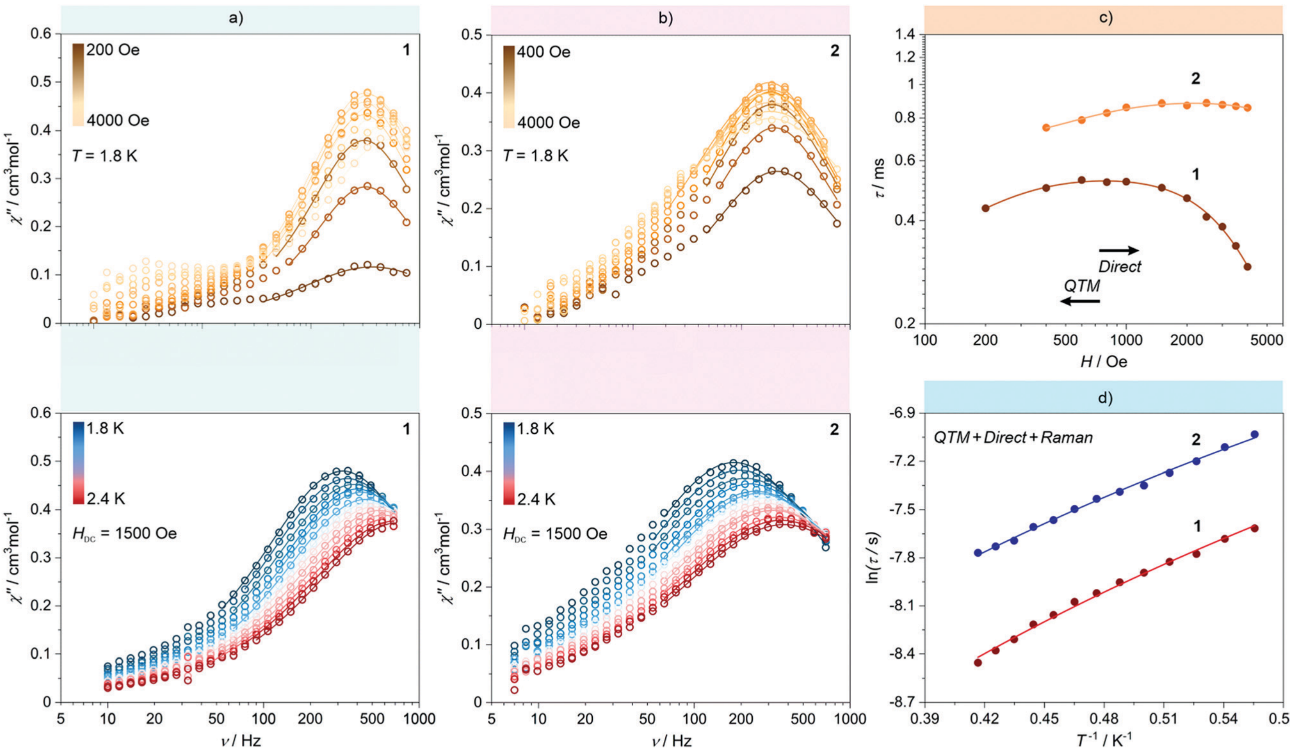

Fig. 5 Representative alternate-current (ac) magnetic characteristics of **1** and **2**: magnetic-field-variable frequency-dependences of out-of-phase magnetic susceptibility, χ_M'' at T = 1.8 K (top) and temperature-variable frequency-dependences of χ_M'' at H_{dc} = 1500 Oe (bottom) for **1** (a) and **2** (b), together with the resulting dc-field-dependence of magnetic relaxation times (c) and the resulting temperature-dependence of magnetic relaxation times (d) for both **1** and **2**. Coloured solid lines depicted in (a) and (b) correspond to the best-fits obtained using the generalized Debye model for a single relaxation process. Coloured solid lines in (c) and (d) represent the best-fit curves obtained considering three magnetic relaxation pathways: a QTM, a Raman process, and a Direct process (see eqn (1) and the text for details).

Fig. S12, S14, ESI†). This indicates the existence of the non-negligible magnetic anisotropy of incorporated Nd^{III} complexes. The optimal dc field of 1500 Oe was estimated based on the field dependences of relaxation time which was plotted by using a generalized Debye model for ac magnetic data at each applied dc field (Fig. 5c). This optimal field appears due to the equilibrium between the QTM effect, dominating at the low field regime, and a field-induced direct process that governs the magnetic relaxation at higher dc fields.[28] Under the optimized dc field, the temperature-variable ac magnetic data of **1** and **2** were examined (Fig. 5a, b and Fig. S13, S15, ESI†). Below the available frequency limit of 1 kHz, the χ'' maxima were detected in the 1.8–2.4 K range. Similarly to the dc-field-variable ac magnetism, the resulting $\chi''(\nu)$, $\chi'(\nu)$, and Argand $\chi''(\chi')$ plots were fitted according to a generalized Debye model. The extracted relaxation times, both of the τ^{-1} *versus H* as well as τ^{-1} *versus T* dependences, were analysed using eqn (1):

$$\tau^{-1}(H,T) = A_{\mathrm{dir}}TH^{m} + \frac{B_1}{1+B_2H^2} + C_{\mathrm{Raman}}T^{n} \qquad (1)$$

The first term in eqn (1) represents the field-induced direct relaxation process (depicted by A_{dir} and m parameters), the second term is related to the QTM effect (depicted by B_1 and B_2 parameters), whereas the last term reflects a two-phonon Raman relaxation pathway (depicted by C_{Raman} and n parameters).[28] The other possible relaxation process, that is the Orbach relaxation occurring for typical SMM systems through one of the higher-lying m_J states of the ground multiplet, was excluded from the consideration by the results of the *ab initio* calculations (see below). The lack of an Orbach relaxation process both in **1** and **2** was also suggested by the rough fitting of the temperature dependences of magnetic relaxation times by using a simple Arrhenius law for the thermally-activated exponential process (Fig. S16, ESI†). It gives the unreasonably low effective energy barriers of 6 and 4 cm^{-1} for **1** and **2**, respectively, indicating that the Orbach process is not represented.[15,28] Therefore, three relaxation routes, QTM, direct, and Raman processes, were taken into account. To avoid over-parametrization, the contributions from the direct process and the QTM effects were extracted from the field dependences of the relaxation time. The following set of best-fit parameters were obtained (Fig. 5c): $A_{\mathrm{dir}} = 5.51(7) \times 10^{-6}\ \mathrm{s^{-1}\ K^{-1}\ Oe^{-2.276}}$, $B_1 = 1388(78)\ \mathrm{s^{-1}}$, $B_2 = 4.91(40) \times 10^{-5}\ \mathrm{Oe^{-2}}$, and $m = 2.276(1)$, with field-independent contribution, $c = 1829(8)\ \mathrm{s^{-1}}$ for **1**, and $A_{\mathrm{dir}} = 2.00(18) \times 10^{-7}\ \mathrm{s^{-1}\ K^{-1}\ Oe^{-2.295}}$, $B_1 = 405(11)\ \mathrm{s^{-1}}$, $B_2 = 4.28(20) \times 10^{-6}\ \mathrm{Oe^{-2}}$, $m = 2.295(10)$, and $c = 1097(3)\ \mathrm{s^{-1}}$ for **2**, respectively. The further fitting of the related temperature dependences (Fig. 5d) results in the following sets of parameters: $C_{\mathrm{Raman}} = 312(2)\ \mathrm{s^{-1}\ K^{-2.997}}$, $n = 2.997(8)$ for **1**, and $C_{\mathrm{Raman}} = 241(1)\ \mathrm{s^{-1}\ K^{-2.604}}$, $n = 2.604(6)$ for **2**. The n power of the Raman relaxation is noticeably far from the expected $n = 9$ for the Kramers ions which can be assigned to the pronounced role of acoustic phonons in the relaxation mechanism.[28,29] Moreover, the evident deviation from the $\tau^{-1} \sim H^4$ dependence expected for a direct process in Kramers ions is rationalized by the non-negligible role of hyperfine interactions which can lead to the decrease of the m power toward the $\tau^{-1} \sim H^2$ behaviour.[28b] Nevertheless, the obtained best-fit parameters indicate that the Nd^{III} complexes in **1** and **2** exhibit the SMM character exhibiting three different slow magnetic relaxation processes (Fig. 5d). The dominant role is played by the Raman relaxation as depicted by the visualized contributions from all relaxation pathways (Fig. S17, ESI†).

The noticeably higher parameters of Raman relaxation, C_{Raman} and n, were found in **1** which effectively leads to faster overall magnetic relaxation. Thus, the higher-performance SMM character is ascribable to the Nd^{III} complexes embedded in W^{IV}-containing **2** rather than Mo^{IV}-based **1**. This Mo-to-W transition substitution effect on the SMM behaviour in $Ln–[M^{IV}(CN)_8]^{4-}$ assemblies is opposite to those observed recently in the Er–Mo/W and Yb–Mo/W coordination chains.[17] This suggests that the role of the exchange of the lighter Mo^{IV} by the heavier W^{IV} centres in the isostructural compounds may depend on the intrinsic single-ion anisotropy of attached lanthanide(3+) ions and their specific electronic structure. In particular, the non-innocent role can be played by the subtle, but presumably critical, structural modification of lanthanide complexes occurring upon the transition metal substitution as was lately proven for the series of $Ho^{III}–[M^{III}(CN)_6]^{3-}$ (M = Co, Rh, Ir) molecular nanomagnets.[7h] This suggestion is still valid even if **1** and **2** reveal mainly the Raman relaxation process through the virtual states as the recent reports indicate that this magnetic relaxation pathway is expected to be also correlated with the single-ion anisotropy of the incorporated 4f metal ions.[28b,29] However, such a correlation is not yet fully explained and certainly is not easily accessible for **1** and **2** due to their complexity related to the presence of three different Nd^{III} complexes of similar but distinguishable magnetic anisotropy (see the *ab initio* calculations below).

Ab initio calculations

To deepen the discussion of the slow magnetic relaxation effects found in **1** and **2**, the CASSCF/RASSI/SINGLE_ANISO *ab initio* calculations of the Nd^{III} crystal-field effect were performed within an OpenMolcas package. The calculations were executed for three crystallographically distinguishable Nd^{III} complexes (Nd1, Nd2, Nd2′, Fig. 1) using the crystal structure of **1a** found from the SC-XRD experiment (Fig. S18, ESI,† see also Table 1 and Tables S7–S13, ESI†). The analysed compound consists of cyanido- and pzdo-bridged coordination layers, thus, for the purpose of calculations, each f-block metal centre was extracted from the framework together with the attached $[Mo^{IV}(CN)_8]^{4-}$ moieties, pzdo and aqua ligands (Fig. S18, ESI†). The *ab initio* calculations were performed using two basis sets, the small and the large one (Table S7, ESI†), leading to the consistent set of results differing mainly in the scale of the whole crystal field splitting (Table S8, ESI†). The obtained composition of the crucial ground Kramers doublets for all three investigated Nd centres, together with the respective components of the pseudo-*g*-tensors, were gathered in Table 1 while a more detailed collection of the results is shown in Tables S8–S10, ESI.† For the nine-coordinated Nd1 and Nd2

Table 1 The selected results of the *ab initio* calculations of the crystal-field effect for Nd^{III} complexes in **1a** (Nd1, Nd2, and Nd2′ complexes; see Fig. 1 and Fig. S18, ESI) obtained within the large (L) basis sets (Table S7, ESI)

Nd^{III} centre		Nd1	Nd2	Nd2′
m_J composition of the ground Kramers doublet (components with $>2\%$ contribution)		±7/2, 73.0% ±5/2, 7.1% ∓7/2, 6.5% ∓5/2, 5.1% ±9/2, 4.4%	±9/2, 65.9% ±1/2, 15.3% ±5/2, 8.7% ∓9/2, 4.4% ±3/2, 2.1%	±9/2, 67.6% ±5/2, 10.2% ±3/2, 8.1% ±7/2, 4.7% ∓9/2, 4.4%
Pseudo-*g*-tensor of the ground doublet	g_x	1.5559	1.0135	0.1845
	g_y	1.6555	1.2071	0.6323
	g_z	4.1478	4.9526	5.4265
The energy gap between the ground and the 1st excited Kramers doublets of the ground multiplet		92.73 cm^{-1}	127.04 cm^{-1}	136.31 cm^{-1}

centres, the impact of the crystal field on the Nd^{III} $^4I_{9/2}$ ground multiplet results in the formation of very different ground states characterized by the main components attributed to $m_J = \pm 7/2$ and $m_J = \pm 9/2$, respectively. This can be correlated with a different shape of the first coordination sphere, which was determined for Nd1 as a tricapped trigonal prism, while Nd2 adopts the geometry of a strongly distorted capped square antiprism (Fig. 1 and Table S2, ESI†). On the other hand, the change from nine-coordinated Nd2 to eight-coordinated Nd2′ centres leaves the contribution of the main m_J component in the ground Kramers doublet almost unchanged. Nevertheless, the resulting ground sub-levels involve large admixtures of the other m_J states, thus their overall magnetic anisotropy is rather weak. The extracted pseudo-*g*-tensors, visualized in Fig. S18, ESI,† are characterized by the large g_z factors but with significant transversal components which generate the strong QTM effect for all investigated Nd^{III} complexes.[5,7] This perfectly agrees with the ac magnetic data indicating the disappearance of the SMM features without the application of an external dc field (Fig. 5).

The results of the *ab initio* calculations exclude also the presence of an Orbach-type relaxation. For Nd1, Nd2, and Nd2′ centres, the first excited Kramers doublets are located at *ca.* 92.7, 127.0, and 136.3 cm^{-1}, respectively (Table 1 and Table S8, ESI†). Such values are much higher than the effective energy barrier of *ca.* 6 cm^{-1}, extracted from the Arrhenius-type temperature dependence of relaxation times (Fig. S16, ESI†). This indicates that the observed *T*-dependence of the overall relaxation time in **1** is dominated by the under-barrier processes such as the Raman relaxation suggested by the thorough analysis of the experimental data (Fig. 5). The same statement is valid for **2** lacking an exact structural model, as the W^{IV}-based analogue is characterized by the similarly low effective energy barrier of *ca.* 4 cm^{-1}. This interpretation is consistent with the latest reports dealing with field-induced SMMs based on weakly anisotropic lanthanide ions, such as Yb^{3+}, lacking the Orbach process in their slow magnetic relaxation effects.[7,9] The results of *ab initio* calculations, including the elucidated crystal-field parameters for all Nd complexes in **1a** (Tables S11–S13, ESI†), enabled the simulation of the representative dc magnetic characteristics which perfectly match the experimental curves for both **1** and **2** (Fig. S11, ESI†). This is additional proof of their similarity from the viewpoint of the f-block metal-centred electronic structure and the related magnetic anisotropy. This also confirms good magnetic isolation of Nd^{III} centres as no sign of noticeable magnetic interactions is observed.

Apart from the ground multiplet composition, the *ab initio* calculations also give information about the energy of the excited states of Ln^{3+} ions. The precision of determination of the absolute energy value for excited terms is more affected by the number and the proximity (in terms of energy) of the other electronic states taken under consideration and optimized during the SA-CASSCF step, thus a direct reproduction of the emission spectra is an extremely difficult task. This is also connected with the lack of geometry optimization for excited states and the neglected role of vibrational modes. However, the splitting of the main experimental emissive transition to the ground multiplet, $^4I_{9/2}$ for Nd^{III}, can be correlated with the calculated crystal field splitting (assuming a small impact of the geometry changes for the well-screened f-electrons) if the measurement temperature is sufficiently lowered to eliminate or at least restrain the influence of hot transitions. Here, despite the presence of three independent Nd^{III} centres in the structure of **1a**, we attempted to correlate the results of the *ab initio* calculations with the high-resolution emission spectra gathered at the relatively low temperature of 77 K (Fig. S19, ESI†). As a result, we obtained a proper match between the emission band located in the 850–900 nm range, which originates from the $^4F_{3/2} \rightarrow {}^4I_{9/2}$ electronic transition, and the energy splitting of each Nd^{III} centre. Such analysis is equally applicable to the emission pattern for **1** and **2**, again confirming a similar electronic structure. However, it should be noted that at 77 K several remaining hot bands are expected, which visibly affects the emission band resolution. Nevertheless, the magneto-optical correlation confirms experimentally the validity of the *ab initio* calculations, particularly from the context of the overall energy scale of the Nd^{III} crystal field effect in **1** and **2**.

Conclusions

Herein, we report unique multifunctional molecular materials combining second-harmonic generation (SHG) activity, sensitized near-infrared (NIR) photoluminescence and the effect of slow relaxation of magnetization. This conjunction of optical and magnetic functionalities was achieved by the formation of

NIR-emissive Nd^{III} molecular nanomagnets within the layered coordination frameworks. Their skeletons employ two types of molecular linkers, organic pyrazine-*N*,*N′*-dioxide and inorganic octacyanido-metallates(IV), whose specific intralayer alignment, supported by the non-covalent anion–π interactions, leads to the non-centrosymmetric crystal structure (Table S5, ESI†). Therefore, in this work, we present the generation of chiral luminescent nanomagnets which takes advantage not only of tunable physical properties of lanthanide(III) complexes but also of the non-innocent role of the attached cyanido metal complex which contributes significantly to the induction of chirality as well as sensitization of the NIR photoluminescence. The application of cyanido metal complexes enables also the modulation of all physical features by the changing of the d-transition metal centre of the cyanido complex. The exchange of Mo^{IV} with W^{IV} enhances the SH intensity, increases the sensitization efficiency at low temperatures, and slowdowns the magnetic relaxation processes. Despite the fact that the mechanisms of these effects are not fully elucidated, it is proven that even the small structural variation related to the Mo-to-W replacement can be an efficient tool for the material performance optimization within both magnetic and optical functionalities. The further functionalization of luminescent single-molecule magnets toward chirality-related non-linear optical and magneto-optical properties using non-innocent cyanido metalloligands is planned. The work on the improvement of single-ion anisotropy of the incorporated lanthanide centres, for instance by inducing the axial alignment of negatively charged ligands expected to be suitable for Nd^{II} centres, should also be considered.[15] Moreover, the obtained compounds consist of neutral coordination layers of the well-recognized SHG, luminescent, and molecular nanomagnetic properties which make them attractive candidates as potential two-dimensional materials processable into the magnetic and optical devices which is worth examining as a next research step.

Experimental section

Materials

Neodymium(III) chloride hexahydrate, pyrazine, and bis(tri-phenylphosphine)iminium chloride were purchased from Sigma-Aldrich and used as received. The $K_4[Mo(CN)_8]\cdot 2H_2O$, $K_4[W(CN)_8]\cdot 2H_2O$, $\{(bpyH)_3(H_3O)[Mo(CN)_8]\cdot H_2O\}$, $\{(bpyH)_3(H_3O)[W(CN)_8]\cdot H_2O\}$, $PPN_4[Mo(CN)_8]\cdot 10H_2O$ and $PPN_4[W(CN)_8]\cdot 10H_2O$ salts, as well as pyrazine-*N*,*N′*-dioxide (pzdo), were synthesized according to modified published procedures.[30] All other reagents were purchased from TCI Chemicals or Sigma-Aldrich and were used without further purification.

Synthetic procedures

Synthesis of 1. 3 mL of a methanolic solution of 17.9 mg (0.05 mmol) of $NdCl_3\cdot 6H_2O$ was rapidly added to the aqueous solution containing 40.6 mg (0.05 mmol) of $\{(bpyH)_3(H_3O)[Mo(CN)_8]\cdot H_2O\}$ and 28.0 mg (0.25 mmol) of pzdo. The resulting mixture was stirred for several seconds and left for crystallization. After three weeks, yellow plate-shaped crystals of **1** (a mixture of two enantiomorphs, **1a** and **1b**, see Fig. 1 and structural studies for details) were obtained. They were filtrated, washed with methanol, and dried overnight. The composition of **1**, $\{[Nd_4(H_2O)_{17}(pzdo)_5][M^{IV}(CN)_8]_3\}\cdot 9H_2O$, was determined by a SC-XRD experiment and confirmed by the CHN elemental analysis and TGA measurements. The P-XRD analysis indicates that the crystals of **1** are stable on air (Fig. 2). Yield: 20.1 mg, 64% (based on Nd). Elem. anal. calcd for $C_{44}H_{72}Mo_3N_{34}Nd_4O_{36}$ (M_W = 2518.03 g mol^{-1}): C, 21.0%; H, 2.9%; N, 18.9%. Found: C, 21.4%; H, 2.7%; N, 18.5%. IR spectrum (Fig. S1, ESI†): bands situated at 2162, 2150, 2139, 2122, and 2107 cm^{-1} indicate the presence of stretching vibrations of cyanido ligands of the $[Mo^{IV}(CN)_8]^{4-}$ anions.[13,14,17]

Synthesis of 2. The compound **2** was obtained in an analogous manner as described for **1** using $\{(bpyH)_3(H_3O)[W(CN)_8]\cdot H_2O\}$ (45 mg, 0.05 mmol) instead of $\{(bpyH)_3(H_3O)[Mo(CN)_8]\cdot H_2O\}$. The mixing of both starting solutions led to the immediate precipitation of an orange suspension that leads to the polycrystalline sample of **2** within a few hours. The P-XRD analysis confirmed the isostructurality of **1** and **2** (Fig. 2). Yield: 14.8 mg, 43% (based on Nd). Elem. anal. calcd. for $C_{44}H_{72}W_3N_{34}Nd_4O_{36}$ (M_W = 2781.73 g mol^{-1}): C, 19.0%; H, 2.6%; N, 17.1%. Found: C, 19.2%; H, 2.4%; N, 17.3%. IR spectrum (Fig. S1, ESI†): bands situated at 2162, 2150, 2136, 2120, and 2104 cm^{-1} indicate the presence of stretching vibrations of cyanido ligands of the $[W^{IV}(CN)_8]^{4-}$ entities.[13,14,17]

Note that both obtained materials, **1** and **2**, can be alternatively obtained starting from $PPN_4[M^{IV}(CN)_8]\cdot 10H_2O$ salts, namely $PPN_4[Mo^{IV}(CN)_8]\cdot 10H_2O$ (131.9 mg, 0.05 mmol) for **1**, and $PPN_4[W^{IV}(CN)_8]\cdot 10H_2O$ (136.3 mg, 0.05 mmol) for **2**, respectively.

X-Ray crystallography

The single crystals of two enantiomorphs of **1**, namely **1a** and **1b**, selected for the SC-XRD experiment were taken directly from the mother solution, covered by Apiezon N grease, and mounted on the Micro Mounts™ holder. The experiment was performed at 100(2) K, using a Bruker D8 Quest Eco Photon50 CMOS diffractometer, equipped with graphite monochromated MoKα radiation. The SAINT and SADABS programs were employed for data reduction and cell refinement processes. The absorption correction was conducted using a multi-scan procedure. The crystal structures were solved by an intrinsic phasing method using a SHELXT programme within the Apex3 package.[31a] The crystal structure refinement was carried out by a weighted full-matrix least-squares method on F^2 of SHELX-2014/7 within the WinGX (ver. 2014.1) software.[31b] All non-hydrogen atoms were refined anisotropically. Hydrogen atoms of water molecules were found from the residual electron density map and refined isotropically. Hydrogen atoms of pzdo ligands were partially calculated on the idealized positions, refined using a riding model, and partially found from the electron density map. Crystals of both **1a** and **1b** reveal significant structural disorder related to the partial occupancy of nine- and eight-coordinated complexes on the Nd2 site, named Nd2 and Nd2′ (Fig. S4, ESI†). Therefore, we found it necessary to apply a series of restraints of the DELU and ISOR type. Additionally, the series of DFIX restraints were applied to non-calculated hydrogen atoms to stabilize their positions and guarantee the convergence of the refinement procedure, in particular for the disordered fragment of the crystal structures. For one of the enantiomers, **1b**, two OMIT commands were used to remove the reflections strongly affected by the X-ray beam. Selected details of crystal data and structure refinement were gathered in Table S1, ESI.† The detailed structure parameters are listed in Table S3, ESI.† CCDC reference numbers are 2061390 and 2061391, for **1a**, and **1b**, respectively.† Powder X-ray diffraction (P-XRD) patterns for **1** and **2** were gathered using a Bruker D8 Advance Eco powder X-ray diffractometer equipped with CuKα radiation source and a capillary spinning add-on. The powder samples were dried in the air and inserted into a glass capillary before the P-XRD measurements which were performed at room temperature. Continuous shape measure analysis for the Mo(IV) and Nd(III) complexes was performed using SHAPE software ver. 2.1.[21] Structural figures were created in the Mercury 4.3.1 software.

Physical techniques

The solid-state UV-Vis-NIR absorption spectra were measured on a Shimadzu UV-3600i-plus spectrophotometer using the thin films of ground samples dispersed in paraffin oil and inserted between quartz plates. IR absorption spectra were collected using a Nicolet iN10 MX FTIR microscope. Elemental analysis was performed using the Elementar Vario Micro Cube CHNS analyser. Thermogravimetric (TG) measurements were performed on a NETZSCH TG 209 F1 Libra apparatus. Solid-state photoluminescence spectra were gathered on a Horiba Jobin-Yvon Fluorolog-3 (FL3-211) spectrofluorimeter equipped with a 450 W Xe lamp and an InGaAs photodiode detector DSS-IGA020L cooled using liquid nitrogen. The data analysis was carried out using FluorEssence® software. Magnetic measurements were conducted using a Quantum Design MPMS-3 Evercool magnetometer. The samples for the magnetic studies were immersed in the mother solution and sealed in a glass tube. Magnetic data include the diamagnetic corrections from the measured materials and the sample holder. Second harmonic generation (SHG) experiments were performed using a homemade optical setup (Fig. S7, ESI†). A 1040 nm femtosecond laser was used as incident fundamental light, which was generated by a Spirit® One™ 1040-8 laser box provided by Spectra-Physics®, with pulse width less than 400 fs, a repetition rate of 200 kHz, and adapted with a pulse picker. After being reflected by dielectric multilayer mirrors, the fundamental laser beam went through a coloured glass filter to cut off the visible component, and then perpendicularly irradiated onto the surface of the sample, which was prepared in the powder pellet form placed in a glass holder. The resulting SH signal was detected in a reflection mode. By applying a harmonic separator and a focal lens, the reflection SHG light was regulated to a monochromator (Oriel® 77250), and then the signal was finally detected by a photomultiplier tube (Hamamatsu R464). Data collection was realized by a customized LabVIEW™ interface which can record the real-time incident laser intensity and the counts-per-second of the detected SH signal. To verify the SHG activity, each sample was characterized by both the power-dependence and the wavelength-dependence measurements. For the first measurement, the incident laser intensity was tuned with a linear increment from zero, while for the latter measurement, the detection wavelength was adjusted by the monochromator. The powder samples of **1** and **2**, being the mixture of enantiomorphic crystals, were investigated in the SHG experiments as the single crystals sufficiently large for the related measurements of SH light could not be isolated. To quantify the SH intensities generated by the investigated samples, a potassium dihydrogen phosphate (KDP) powder pellet was used as a reference sample.

Computational details

The *ab initio* calculations were performed for molecular moieties based on three symmetry independent coordination complexes of Nd1, Nd2 and Nd2′, and the geometries were taken from the single-crystal X-ray diffraction experiment for **1a**. All the discussed molecular fragments are visualized together with the calculated anisotropy axes in Fig. S18, ESI.† Apart from Nd^{III} centres, each moiety contains all the organic and aqua ligands, and all nearest diamagnetic octacyanidometallate units. To examine local magnetic properties of Nd^{III}, State Average Complete Active Space Self-Consistent Field (SA-CASSCF) calculations were performed using the OpenMolcas software.[32] Scalar relativistic effects were taken into account by employing two-component second-order Douglas–Kroll–Hess (DKH2) Hamiltonian together with the relativistic Atomic Natural Orbital basis sets of the ANO-RCC type.[33] To save the disk space for computations of such relatively big moieties, Cholesky decomposition of ERI-s (electron repulsion integrals) was used with a 1.0×10^{-8} threshold. Two models were considered: the first one – smaller (S) – with VDZP basis function quality for Nd^{III} and VDZ for other atoms, and – larger (L) – using VTZP for Nd^{III} centres, VDZP for atoms directly bonded to the paramagnetic centre, and VDZ for the others (Table S7, ESI†). In the CASSCF step, the active space was composed of seven 4f orbitals of Nd^{III} with 3 active electrons – CAS (3 in 7), and 35 quartets with 112 doublets spin-adapted states arising from different possible electron distributions in 4f orbitals were evaluated. In the next step, all previously optimized, as spin-free, states were mixed within the Restricted Active Space State Interaction (RASSI) submodule by Spin–Orbit Coupling (SOC) within the atomic mean-field (AMFI) approximation.[34] In the final step, the resulting 364 spin–orbit states were analysed using the SINGLE_ANISO module to obtain main magnetic axes and pseudo-*g*-tensors of each Kramers doublet, simulate $\chi_M T(T)$ and $M(H)$ magnetic characteristics, and decompose spin–orbit states into such with a definite projection of the total momentum on the located quantization *z*-axis.[35] The energy splitting of the ground $^4I_{9/2}$ multiplets of all three calculated Nd^{III} complexes along with the pseudo-*g*-tensor components and the composition of the ground doublet in the m_J basis are shown in Table 1 and Tables S8–S10 (ESI†).

Conflicts of interest

There are no conflicts to declare.

Acknowledgements

This work was financed by the National Science Centre, Poland within the OPUS-14 project, grant no. 2017/27/B/ST5/00947, and by the Polish Ministry of Science and Higher Education within the ''Diamond Grant'' program, no. DI2018 017848.

References

1 (*a*) R. Sessoli, D. Gatteschi, A. Caneschi and M. A. Novak, *Nature*, 1993, **365**, 141; (*b*) F.-S. Guo, B. M. Day, Y.-C. Chen, M.-L. Tong, A. Mansikkamäki and R. A. Layfield, *Science*, 2018, **362**, 1400.

2 (*a*) R. Marin, G. Brunet and M. Murugesu, *Angew. Chem., Int. Ed.*, 2021, **60**, 1728; (*b*) S. M. Aldoshin, D. V. Korchagin, A. V. Palii and B. S. Tsukerblat, *Pure Appl. Chem.*, 2017, **89**, 1119; (*c*) J. M. Frost, K. L. M. Harriman and M. Murugesu, *Chem. Sci.*, 2016, **7**, 2470; (*d*) M. Mannini, F. Pineider, P. Sainctavit, C. Danieli, E. Otero, C. Sciancalepore, A. M. Talarico, M.-A. Arrio, A. Cornia, D. Gatteschi and R. Sessoli, *Nat. Mater.*, 2009, **8**, 194; (*e*) L. Bogani and W. Wernsdorfer, *Nat. Mater.*, 2008, **7**, 179.

3 (*a*) D. Gatteschi and R. Sessoli, *Angew. Chem., Int. Ed.*, 2003, **42**, 268; (*b*) K. S. Pedersen, A.-M. Ariciu, S. McAdams, H. Weihe, J. Bendix, F. Tuna and S. Piligkos, *J. Am. Chem. Soc.*, 2016, **138**, 5801; (*c*) L. Escalera-Moreno, J. J. Baldoví, A. Gaita-Ariño and E. Coronado, *Chem. Sci.*, 2018, **9**, 3265; (*d*) E. Coronado, *Nat. Rev. Mater.*, 2020, **5**, 87.

4 N. Ishikawa, M. Sugita, T. Ishikawa, S. Koshihara and Y. Kaizu, *J. Am. Chem. Soc.*, 2003, **125**, 8694.

5 (*a*) D. N. Woodruff, R. E. P. Winpenny and R. A. Layfield, *Chem. Rev.*, 2013, **113**, 5110; (*b*) F. Pointillart, O. Cador, B. Le Guennic and L. Ouahab, *Coord. Chem. Rev.*, 2017, **346**, 150; (*c*) L. Ungur and L. F. Chibotaru, *Inorg. Chem.*, 2016, **55**, 10043; (*d*) J. Lu, M. Guo and J. Tang, *Chem. – Asian J.*, 2017, **12**, 2772; (*e*) Z. Zhu, M. Guo, X.-L. Li and J. Tang, *Coord. Chem. Rev.*, 2019, **378**, 350; (*f*) C.-L. Yin, Z.-B. Hu, Q.-Q. Long, H.-S. Wang, J. Li, Y. Song, Z.-C. Zhang, Y.-Q. Zhang and Z.-Q. Pan, *Dalton Trans.*, 2019, **48**, 512; (*g*) H.-S. Wang, C.-L. Yin, Z.-B. Hu, Y. Chen, Z.-Q. Pan, Y. Song, Y.-Q. Zhang and Z.-C. Zhang, *Dalton Trans.*, 2019, **48**, 10011; (*h*) H.-S. Wang, K. Zhang, Y. Song and Z.-Q. Pan, *Inorg. Chim. Acta*, 2021, **521**, 120318.

6 (*a*) Y. Bi, X.-T. Wang, W. Liao, X. Wang, R. Deng, H. Zhang and S. Gao, *Inorg. Chem.*, 2009, **48**, 11743; (*b*) J. Long, Y. Guari, R. A. S. Ferreira, L. D. Carlos and J. Larionova, *Coord. Chem. Rev.*, 2018, **363**, 57; (*c*) J.-H. Jia, Q.-W. Li, Y.-C. Chen, J.-L. Liu and M.-L. Tong, *Coord. Chem. Rev.*, 2019, **378**, 365; (*d*) J. Long, *Front. Chem.*, 2019, **7**, 63; (*e*) Z. Zhu, X.-L. Li, S. Liu and J. Tang, *Inorg. Chem. Front.*, 2020, **7**, 3315.

7 (*a*) C.-S. Liu, M. Du, E. C. Sañudo, J. Echeverria, M. Hu, Q. Zhang, L.-M. Zhou and S.-M. Fang, *Dalton Trans.*, 2011, **40**, 9366; (*b*) J.-R. Jiménez, I. F. Díaz-Ortega, E. Ruiz, D. Aravena, S. J. A. Pope, E. Colacio and J. M. Herrera, *Chem. – Eur. J.*, 2016, **22**, 1454; (*c*) G. Cucinotta, M. Perfetti, J. Luzon, M. Etienne, P.-E. Car, A. Caneschi, G. Calvez, K. Bernot and R. Sessoli, *Angew. Chem., Int. Ed.*, 2012, **51**, 1606; (*d*) J. Long, R. Vallat, R. A. S. Ferreira, L. D. Carlos, F. A. Almeida Paz, Y. Guari and J. Larionova, *Chem. Commun.*, 2012, **48**, 9974; (*e*) K. S. Pedersen, J. Dreiser, H. Weihe, R. Sibille, H. V. Johannesen, M. A. Sørensen, B. E. Nielsen, M. Sigrist, H. Mutka, S. Rols, J. Bendix and S. Piligkos, *Inorg. Chem.*, 2015, **54**, 7600; (*f*) P. Martín-Ramos, J. T. Coutinho, M. Ramos Silva, L. C. J. Pereira, F. Lahoz, P. S. Pereira da Silva, V. Lavín and J. Martín-Gil, *New J. Chem.*, 2015, **39**, 1703; (*g*) K. Yamashita, R. Miyazaki, Y. Kataoka, T. Nakanishi, Y. Hasegawa, M. Nakano, T. Yamamura and T. Kajiwara, *Dalton Trans.*, 2013, **42**, 1987; (*h*) J. Wang, J. J. Zakrzewski, M. Zychowicz, V. Vieru, L. F. Chibotaru, K. Nakabayashi, S. Chorazy and S. Ohkoshi, *Chem. Sci.*, 2021, **12**, 730.

8 (*a*) Y. Bi, C. Chen, Y.-F. Zhao, Y.-Q. Zhang, S.-D. Jiang, B.-W. Wang, J.-B. Han, J.-L. Sun, Z.-Q. Bian, Z.-M. Wang and S. Gao, *Chem. Sci.*, 2016, **7**, 5020; (*b*) D. Errulat, R. Marin, D. A. Gálico, K. L. M. Harriman, A. Pialat, B. Gabidullin, F. Iikawa, O. D. D. Couto, Jr., J. O. Moilanen, E. Hemmer, F. A. Sigoli and M. Murugesu, *ACS Cent. Sci.*, 2019, **5**, 1187.

9 (*a*) J. Wang, J. J. Zakrzewski, M. Heczko, M. Zychowicz, K. Nakagawa, K. Nakabayashi, B. Sieklucka, S. Chorazy and S. Ohkoshi, *J. Am. Chem. Soc.*, 2020, **142**, 3970; (*b*) J. Long, J. Rouquette, J.-M. Thibaud, R. A. S. Ferreira, L. D. Carlos, B. Donnadieu, V. Vieru, L. F. Chibotaru, L. Konczewicz, J. Haines, Y. Guari and J. Larionova, *Angew. Chem., Int. Ed.*, 2015, **127**, 2264; (*c*) P.-H. Guo, J.-L. Liu, J.-H. Jia, J. Wang, F.-S. Guo, Y.-C. Chen, W.-Q. Lin, J.-D. Leng, D.-H. Bao, X.-D. Zhang, J.-H. Luo and M.-L. Tong, *Chem. – Eur. J.*, 2013, **19**, 8769; (*d*) P.-H. Guo, Y. Meng, Y.-C. Chen, Q.-W. Li, B.-Y. Wang, J.-D. Leng, D.-H. Bao, J.-H. Jia and M.-L. Tong, *J. Mater. Chem. C*, 2014, **2**, 8858; (*e*) S.-D. Zhu, J.-J. Hu, L. Dong, H.-R. Wen, S.-J. Liu, Y.-B. Lu and C.-M. Liu, *J. Mater. Chem. C*, 2020, **8**, 16032.

10 (*a*) A. Ould-Hamouda, A. Iazzolino, H. Tokoro, S. Ohkoshi and E. Freysz, *Eur. J. Inorg. Chem.*, 2018, 378; (*b*) M. Komine, K. Imoto, Y. Miyamoto, K. Nakabayashi and S. Ohkoshi, *Eur. J. Inorg. Chem.*, 2018, 1367.

11 (*a*) J. Zhao, T. Zhang, X.-Y. Dong, M.-E. Sun, C. Zhang, X. Li, Y. S. Zhao and S.-Q. Zang, *J. Am. Chem. Soc.*, 2019, **141**, 15755; (*b*) J. Zhang, L. Dai, A. M. Webster, W. T. K. Chan, L. E. Mackenzie, R. Pal, S. L. Cobb and G.-L. Law, *Angew. Chem., Int. Ed.*, 2021, **60**, 1004.

12 (*a*) G. L. J. A. Rikken and E. Raupach, *Nature*, 1997, **390**, 493; (*b*) C. Train, M. Gruselle and M. Verdaguer, *Chem. Soc. Rev.*, 2011, **40**, 3297.

13 (*a*) S. Chorazy, M. Wyczesany and B. Sieklucka, *Molecules*, 2017, **22**, 1902; (*b*) J. J. Zakrzewski, M. Liberka, M. Zychowicz and S. Chorazy, *Inorg. Chem. Front.*, 2021, **8**, 452; (*c*) Y. Xin, J. Wang, M. Zychowicz, J. J. Zakrzewski, K. Nakabayashi, B. Sieklucka, S. Chorazy and S. Ohkoshi, *J. Am. Chem. Soc.*, 2019, **141**, 18211; (*d*) J. J. Zakrzewski, B. Sieklucka and S. Chorazy, *Inorg. Chem.*, 2020, **59**, 1393; (*e*) P. A. Smith, C. Crawford, N. Beedoe, Z. Assefa and R. E. Sykora, *Inorg. Chem.*, 2012, **51**, 12230; (*f*) R. J. Roberts, D. Le and D. B. Leznoff, *Inorg. Chem.*, 2017, **56**, 7948.

14 (*a*) S. Chorazy, J. J. Zakrzewski, M. Magott, T. Korzeniak, B. Nowicka, D. Pinkowicz, R. Podgajny and B. Sieklucka, *Chem. Soc. Rev.*, 2020, **49**, 5945; (*b*) D. Pinkowicz, R. Podgajny, W. Nitek, M. Rams, A. M. Majcher, T. Nuida, S. Ohkoshi and B. Sieklucka, *Chem. Mater.*, 2011, **23**, 21; (*c*) M. Atzori, I. Breslavetz, K. Paillot, K. Inoue, G. L. J. A. Rikken and C. Train, *J. Am. Chem. Soc.*, 2019, **141**, 20022; (*d*) J. J. Zakrzewski, S. Chorazy, K. Nakabayashi, S. Ohkoshi and B. Sieklucka, *Chem. – Eur. J.*, 2019, **25**, 11820; (*e*) M. Liberka, J. Kobylarczyk, T. M. Muziol, S. Ohkoshi, S. Chorazy and R. Podgajny, *Inorg. Chem. Front.*, 2019, **6**, 3104; (*f*) S. Ohkoshi, K. Nakagawa, K. Imoto, H. Tokoro, Y. Shibata, K. Okamoto, Y. Miyamoto, M. Komine, M. Yoshikiyo and A. Namai, *Nat. Chem.*, 2020, **12**, 338.

15 (*a*) S. K. Gupta, T. Rajeshkumar, G. Rajaraman and R. Murugavel, *Chem. Commun.*, 2016, **52**, 7168; (*b*) H. Wada, S. Ooka, T. Yamamura and T. Kajiwara, *Inorg. Chem.*, 2017, **56**, 147; (*c*) Y.-C. Chen, X.-S. Huang, J.-L. Liu and M.-L. Tong, *Inorg. Chem.*, 2018, **57**, 1178; (*d*) H. Ke, L. Zhao, Y. Guo and J. Tang, *Dalton Trans.*, 2012, **41**, 2314; (*e*) J. Liu, D. Reta, J. A. Cleghorn, Y. X. Yeoh, F. Ortu, C. A. P. Goodwin, N. F. Chilton and D. P. Mills, *Chem. – Eur. J.*, 2019, **25**, 7749.

16 (*a*) J.-C. G. Bünzli and C. Piguet, *Chem. Soc. Rev.*, 2005, **34**, 1048; (*b*) S. V. Eliseeva and J.-C. G. Bünzli, *Chem. Soc. Rev.*, 2010, **39**, 189.

17 R. Jankowski, J. J. Zakrzewski, O. Surma, S. Ohkoshi, S. Chorazy and B. Sieklucka, *Inorg. Chem. Front.*, 2019, **6**, 2423.

18 L. Pérez-García and D. B. Amabilino, *Chem. Soc. Rev.*, 2002, **31**, 342.

19 (*a*) S. Ohkoshi, S. Takano, K. Imoto, M. Yoshikiyo, A. Namai and H. Tokoro, *Nat. Photonics*, 2014, **8**, 65; (*b*) T. Ohno, S. Chorazy, K. Imoto and S. Ohkoshi, *Cryst. Growth Des.*, 2016, **16**, 4119.

20 R. Podgajny, D. Pinkowicz, B. Czarnecki, M. Kozieł, S. Chorazy, M. Wis, W. Nitek, M. Rams and B. Sieklucka, *Cryst. Growth Des.*, 2014, **14**, 4030.

21 (*a*) M. Llunell, D. Casanova, J. Cirera, J. Bofill, P. Alemany, S. Alvarez, M. Pinsky and D. Avnir, *SHAPE v. 2.1, Program for the Calculation of Continuous Shape Measures of Polygonal and Polyhedral Molecular Fragments*, University of Barcelona, Barcelona, Spain, 2013; (*b*) D. Casanova, J. Cirera, M. Llunell, P. Alemany, D. Avnir and S. Alvarez, *J. Am. Chem. Soc.*, 2004, **126**, 1755.

22 (*a*) A. Altomare, C. Cuocci, C. Giacovazzo, A. Moliterni, R. Rizzi, N. Corriero and A. Falcicchio, *J. Appl. Crystallogr.*, 2013, **46**, 1231; (*b*) A. Altomare, C. Giacovazzo, A. Guagliardi, A. G. G. Moliterni, R. Rizzi and P.-E. Werner, *J. Appl. Crystallogr.*, 2000, **33**, 1180; (*c*) A. Boultif and D. Louër, *J. Appl. Crystallogr.*, 2004, **37**, 724.

23 L. Bonacina, P.-F. Brevet, M. Finazzi and M. Celebrano, *J. Appl. Phys.*, 2020, **127**, 230901.

24 (*a*) P.-X. Li, C.-L. Hu, X. Xu, R.-Y. Wang, C.-F. Sun and J.-G. Mao, *Inorg. Chem.*, 2010, **49**, 4599; (*b*) P. A. Maggard, X. Cheng, S. Deng and M.-H. Whangbo, *Molecules*, 2020, **25**, 867; (*c*) M. Komine, K. Imoto, A. Namai, M. Yoshikiyo and S. Ohkoshi, *Inorg. Chem.*, 2021, **60**, 2097.

25 (*a*) O. Savchuk, J. J. Carvajal, L. G. De la Cruz, P. Haro-Gonzalez, M. Aguilo and F. Diaz, *J. Mater. Chem. C*, 2016, **4**, 7397; (*b*) S. Chorazy, B. Sieklucka and S. Ohkoshi, *Cryst. Growth Des.*, 2016, **16**, 4918; (*c*) B. S. K. Chong and E. G. Moore, *Inorg. Chem.*, 2018, **57**, 14062; (*d*) R. E. Rojas-Hernandez, F. Rubio-Marcos, G. Gorni, C. Marini, M. Danilson, L. Pascual, R. U. Ichikawa, I. Hussainova and J. F. Fernandez, *J. Mater. Chem. C*, 2021, **9**, 657.

26 (*a*) J. Del Bene and H. H. Jaffe, *J. Chem. Phys.*, 1968, **49**, 1221; (*b*) M. F. A. Hendrickx, V. S. Mironov, L. F. Chibotaru and A. Ceulemans, *Inorg. Chem.*, 2004, **43**, 3142.

27 (*a*) F. R. Goncalves e Silva, O. L. Malta, C. Reinhard, H.-U. Güdel, C. Piguet, J. E. Moser and J.-C. G. Bünzli, *J. Phys. Chem. A*, 2002, **106**, 1670; (*b*) D. Wu, W. Xiao, L. Zhang, X. Zhang, Z. Hao, G.-H. Pan, Y. Luo and J. Zhang, *J. Mater. Chem. C*, 2017, **5**, 11910; (*c*) K. Kumar, S. Chorazy, K. Nakabayashi, H. Sato, B. Sieklucka and S. Ohkoshi, *J. Mater. Chem. C*, 2018, **6**, 8372.

28 (*a*) S. T. Liddle and J. van Slageren, *Chem. Soc. Rev.*, 2015, **44**, 6655; (*b*) Y.-S. Ding, K.-X. Yu, D. Reta, F. Ortu, R. E. P. Winpenny, Y.-Z. Zheng and N. F. Chilton, *Nat. Commun.*, 2018, **9**, 3134; (*c*) D. Aravena and E. Ruiz, *Dalton Trans.*, 2020, **49**, 9916.

29 (*a*) K. N. Shrivastava, *Phys. Status Solidi B*, 1983, **117**, 437; (*b*) E. Lucaccini, L. Sorace, M. Perfetti, J.-P. Costes and R. Sessoli, *Chem. Commun.*, 2014, **50**, 1648; (*c*) A. B. Canaj, S. Dey, C. Wilson, O. Céspedes, G. Rajaraman and M. Murrie, *Chem. Commun.*, 2020, **56**, 12037; (*d*) A. Chiesa, F. Cugini, R. Hussain, E. Macaluso, G. Allodi, E. Garlatti, M. Giansiracusa, C. A. P. Goodwin, F. Ortu, D. Reta, J. M. Skelton, T. Guidi, P. Santini, M. Solzi, R. De Renzi, D. P. Mills, N. F. Chilton and S. Carretta, *Phys. Rev. B*, 2020, **101**, 174402.

30 (*a*) J. Szklarzewicz, D. Matoga and K. Lewiński, *Inorg. Chim. Acta*, 2007, **360**, 2002; (*b*) D. Matoga, J. Szklarzewicz and M. Mikuriya, *Inorg. Chem.*, 2006, **45**, 7100; (*c*) J. Szklarzewicz, A. Samotus and A. Kanas, *Polyhedron*, 1986, **5**, 1733; (*d*) D. A. Cauzzi, G. Mori, G. Predieri, A. Tripicchio and F. Cavatorta, *Inorg. Chim. Acta*, 1993, **204**, 181;

(*e*) R. Podgajny, D. Pinkowicz, T. Korzeniak, W. Nitek, M. Rams and B. Sieklucka, *Inorg. Chem.*, 2007, **46**, 10416.

31 (*a*) G. M. Sheldrick, *Acta Crystallogr., Sect. A: Found. Adv.*, 2015, **71**, 3; (*b*) L. J. Farrugia, *J. Appl. Crystallogr.*, 2012, **45**, 849.

32 I. F. Galván, M. Vacher, A. Alavi, C. Angeli, F. Aquilante, J. Autschbach, J. J. Bao, S. I. Bokarev, N. A. Bogdanov, R. K. Carlson, L. F. Chibotaru, J. Creutzberg, N. Dattani, M. G. Delcey, S. S. Dong, A. Dreuw, L. Freitag, L. M. Frutos, L. Gagliardi, F. Gendron, A. Giussani, L. González, G. Grell, M. Guo, C. E. Hoyer, M. Johansson, S. Keller, S. Knecht, G. Kovačević, E. Källman, G. L. Manni, M. Lundberg, Y. Ma, S. Mai, J. P. Malhado, P. Å. Malmqvist, P. Marquetand, S. A. Mewes, J. Norell, M. Olivucci, M. Oppel, Q. M. Phung, K. Pierloot, F. Plasser, M. Reiher, A. M. Sand, I. Schapiro, P. Sharma, C. J. Stein, L. K. Sørensen, D. G. Truhlar, M. Ugandi, L. Ungur, A. Valentini, S. Vancoillie, V. Veryazov, O. Weser, T. A. Wesołowski, P.-O. Widmark, S. Wouters, A. Zech, J. P. Zobel and R. Lindh, *J. Chem. Theory Comput.*, 2019, **15**, 5925.

33 (*a*) B. O. Roos, R. Lindh, P.-Å. Malmqvist, V. Veryazov and P.-O. Widmark, *J. Phys. Chem. A*, 2004, **108**, 2851; (*b*) B. O. Roos, R. Lindh, P.-Å. Malmqvist, V. Veryazov and P.-O. Widmark, *J. Phys. Chem. A*, 2005, **109**, 6575; (*c*) B. O. Roos, R. Lindh, P.-Å. Malmqvist, V. Veryazov, P.-O. Widmark and A. C. Borin, *J. Phys. Chem. A*, 2008, **112**, 11431.

34 (*a*) P.-Å. Malmqvist, B. O. Roos and B. Schimmelpfennig, *Chem. Phys. Lett.*, 2002, **357**, 230; (*b*) B. A. Heß, C. M. Marian, U. Wahlgren and O. A. Gropen, *Chem. Phys. Lett.*, 1996, **251**, 365.

35 (*a*) L. F. Chibotaru and L. Ungur, *J. Chem. Phys.*, 2012, **137**, 064112; (*b*) L. Ungur and L. F. Chibotaru, *Chem. – Eur. J.*, 2017, **23**, 3708.